

# Atomistic Simulations for Reactions and Spectroscopy in the Era of Machine Learning

- *Quo Vadis?*

Markus Meuwly\*

*Department of Chemistry, University of Basel, Klingelbergstrasse 80, 4056 Basel, Switzerland*

E-mail: m.meuwly@unibas.ch

January 12, 2022

## Abstract

Atomistic simulations using accurate energy functions can provide molecular-level insight into functional motions of molecules in the gas- and in the condensed phase. Together with recently developed and currently pursued efforts in integrating and combining this with machine learning techniques provides a unique opportunity to bring such dynamics simulations closer to reality. This perspective delineates the present status of the field from efforts of others in the field and some of your own work and discusses open questions and future prospects.

## Introduction

“Atomistic Simulations” provide molecular-level information into chemical and biological phenomena. This is largely due to the possibility to explicitly follow the dynamics of molecular systems with the full information about observables contained in the time series of

positions and velocities. The “translation” between the output from a molecular dynamics (MD) simulation (positions and velocities as a function of time) is accomplished by virtue of statistical mechanics, in particular the correlation function formalism introduced in the 1960s by Zwanzig<sup>1</sup> and Gordon.<sup>2</sup>

The nuclear dynamics - whether described at a classical or at a quantum level - is primarily governed by the underlying energy function  $V(\vec{x})$  where  $\vec{x}$  encompasses all  $3N$  coordinates of an  $N$ -particle system. Most rigorous for such studies will be to use an exact or near-exact solution of the electronic Schrödinger equation together with corresponding forces for each configuration  $\vec{x}$ . Doing this “on the fly” is typically not possible except for systems with a small number of electrons, and not on extended time scales. Hence, such *ab initio* MD (AIMD) methods often use approximations at the density functional theory (DFT) or semiempirical level of theory and typically within a mixed quantum mechanics/molecular mechanics (QM/MM) framework.<sup>3,4</sup>

Since about 10 years the field of computational and theoretical chemistry has seen a profound change in how we think about inter- and intra-molecular interactions. One milestone has been the realization that with a sufficient number of samples the explicit solution of the electronic Schrödinger equation can be replaced by a data-driven approach based on machine learning (ML).<sup>5</sup> This approach consistently applies principles rooted in statistical learning theory.<sup>6</sup> A recent series of reviews delineates the present state of the art of ML-based methods for force fields,<sup>7</sup> for small molecules,<sup>8</sup> and for chemical reactions.<sup>9</sup> It is of interest to mention that for intermolecular interactions such ML-based methods have been used for a considerably longer time,<sup>10,11</sup> especially for triatomics,<sup>12</sup> based on early work by Aronszajn on reproducing kernel Hilbert spaces (RKHS).<sup>13</sup>

One of the particular benefits of atomistic simulations in the context of experiments is the

possibility to relate observables with particular structural features of a system. A topical example concerns infrared (IR) spectroscopy for gas- or condensed-phase systems. At ambient conditions even small peptides sample different conformations each of which exhibits potentially conformer-specific IR spectra. This applies to both, experiments in the gas phase and in solution.<sup>14-16</sup> The question thus arises to what conformational substate a particular set of spectral lines belongs and whether a unique correspondence between structure and spectroscopy can be obtained. However, assigning the spectroscopic features to a particular conformational substate remains a challenge. One possibility to address this problem consists in carrying out extensive electronic structure calculations which, however, are time consuming and usually only applicable to gas-phase systems. Alternatively, MD simulations with improved force fields can be used to determine the underlying structural features by comparing computed and experimentally measured IR spectra.<sup>17,18</sup>

Similarly, a beneficial interplay between experiment and computation has clarified the relationship between structure and spectroscopy for protonated water clusters.<sup>19-21</sup> Often, such experiments are carried out in a supersonic jet combined with mass selection of particular cluster sizes which generates an ensemble of structures that is probed by light. As there is a distribution of cluster geometries that is frozen in the expansion, the spectroscopic signatures are those of a number of - typically - low-energy isomers and not of one single conformer. What spectral features belong to one particular conformation can be clarified by using hole-burning experiments<sup>22</sup> and conformer-specific spectra are then determined from electronic structure calculations. Such an approach has proven very powerful, in particular for small protonated water clusters.<sup>23,24</sup> Very recently, the infrared spectroscopy of  $\text{H}^+(\text{H}_2\text{O})_{21}$  was assigned to particular structural features using Second-order Vibrational Quasi-Degenerate Perturbation Theory (VQDPT2). Based on the agreement between experiment and simulations particular features in the experimental spectra in the high-frequency (OH-stretch) region could be assigned to specific bonding patterns in the protonated water cluster.

Combining computational and experimental approaches is also valuable for chemical reactions in the gas and in the condensed phase. Typical questions arising in this context are A) whether reactions proceed stepwise or concerted, e.g. for phosphate transfer,<sup>25-27</sup> Menshutkin-type,<sup>28-33</sup> or Diels-Alder reactions,<sup>34-37</sup> or B) for unimolecular reactions whether I) decomposition involves one or several competing routes, II) a potential barrier is involved, III) it simply progresses by stretching a chemical bond until it breaks, or IV) a combination of II) and III) is at play which was coined “roaming”.<sup>38</sup> Also, competing pathways can occur and have been found from atomistic simulations.<sup>39-41</sup>

In what follows an account of the status and future prospects of atomistic simulations with a particular focus on classical MD simulations in the context of experiments is given. Findings and relevant advances from recent studies in our group and others in the field are highlighted and open questions that require and spur future developments are formulated and discussed.

## Vibrational Spectroscopy

Optical spectroscopy is a versatile and powerful method to interrogate and characterize the structural dynamics of systems in the gas<sup>42,43</sup> and in the condensed phase.<sup>44-49</sup> It has been proposed (for a cyano-substituted ligand bound to WT and mutant human aldose reductase)<sup>50</sup> and explicitly demonstrated by simulations (for cyano-benzene bound to lysozyme)<sup>51</sup> that IR spectroscopy can be used to infer ligand binding in particular protein pockets. The possibility to relate changes in the infrared spectroscopy with changes in intermolecular binding modes and/or interaction strengths is an exciting prospect for functional studies of biomolecules under realistic conditions, including solvent and ions.

One application of vibrational spectroscopy is positionally resolved infrared spectroscopy to

relate structural features and local/global dynamics with spectroscopic responses. For this, suitable spectroscopic probes are required. One such label is azidohomoalanine (AHA)<sup>52</sup> for which experiments demonstrated that it can be used for site-specific information on the recognition site between the PDZ2 domain and its binding partner.<sup>53</sup> AHA absorbs at around  $\sim 2100 \text{ cm}^{-1}$  with a substantial extinction coefficient ( $\sim 400 \text{ M}^{-1}\text{cm}^{-1}$ ).<sup>52</sup> Attaching  $-\text{N}_3$  to alanine (to give  $\text{AlaN}_3$ ) or AHA and incorporation at almost any position of a protein has been demonstrated following known expression techniques.<sup>54</sup> Furthermore, attachment of an  $-\text{N}_3$  probe is a spatially small modification and the chemical perturbations induced are expected to be small. This makes  $\text{AlaN}_3$  and AHA worthwhile modifications to probe local protein dynamics.

Exhaustive labeling of all 14 alanine residues in WT human Lysozyme provided dynamical information in a position-resolved manner.<sup>55</sup> These simulations were carried out with a conventional protein force field but the energetics of the spectroscopic reporter ( $\text{N}_3^-$ ) was a reproducing kernel Hilbert space<sup>56,57</sup> based on high-level PNO-LCCSD(T)-F12<sup>58,59</sup> calculations together with the aug-cc-pVTZ basis set. This is akin to a mixed quantum mechanics/molecular mechanics (QM/MM) procedure with the advantage that a) evaluating the RKHS is computationally similarly efficient as computing energies and forces for an empirical force field which allows to carry out multi-nanosecond simulations for such a system and b) the quality of the RKHS is that of the underlying quantum chemical method.

Using the same force field for the azide probe attached to every alanine residue in Lysozyme leads to frequency maxima covering a range of  $\sim 15 \text{ cm}^{-1}$ .<sup>55</sup> This compares favourably with an experimentally reported frequency span of  $\sim 10 \text{ cm}^{-1}$  for replacements of Val, Ala, or Glu by AHA in the PDZ2 domain.<sup>52</sup> The frequency fluctuation correlation functions (FFCFs) for the  $\text{N}_3^-$  asymmetric stretch mode decay on two time scales. One is in the sub-picosecond regime and quite universal at  $\tau_1 \sim 0.1 \text{ ps}$  whereas the longer decay time ranges from  $\sim 1$

to  $\sim 10$  ps depending on the position of the label. Experimentally, correlation times of 3 ps have been measured for AHA.<sup>52</sup> Another relevant experimental observable is the inhomogeneous contribution which arises from dynamics that relaxes on time scales longer than  $\tau_2$ . Interestingly, the magnitude of the static component was found to correlate qualitatively with the degree of hydration of the spectroscopic probe.<sup>55</sup>

Another application of simulation and experimental approaches for vibrational spectroscopy is the characterization of the conformational ensemble sampled by peptides and proteins. A widely studied model system in this context is trialanine (Ala<sub>3</sub>).<sup>17,18,60-69</sup> The conformational ensemble from most of the investigations is dominated by the poly-proline II (ppII) structure, often followed by a  $\beta$ -sheet conformation and more rarely some right-handed  $\alpha$ -helical structure. In a notable combined experimental and simulation study the infrared spectroscopy in the amide-I region was used to refine the conformational ensemble. This was done by Bayesian ensemble refinement of the conformational ensemble such as to best reproduce the experimentally measure IR spectra.<sup>17</sup> The refinement effectively reweights a reference distribution with associated basin-specific IR spectra to better describe the experimentally observed spectra. Interestingly, comparable changes in the conformational ensemble were found when going from a conventional point charge force field to a multipolar representation of the amide group although the ppII structure is probably overstabilized in these simulations.<sup>18</sup>

Such studies lay the foundation for more functionally relevant studies of biomolecules such as the A $\beta$  amyloids or insulin. 1d- and 2d-infrared spectroscopy have been used to probe structural features and the dynamics of different amyloids.<sup>70</sup> One distinguishing feature of the 1-dimensional spectra is a narrow, intense absorption between 1615 and 1630  $\text{cm}^{-1}$  which is shifted to the red of the typical  $\beta$ -sheet amide-I bands. Heavy atom labeling of individual -CO groups allows to assign the spectroscopic response to particular parts of the protein.

Using isotope labeling together with 2d-IR spectroscopy and computed spectra from MD simulations allowed to distinguish between a  $\beta$ -arch and a  $\beta$ -turn configuration of polyQ fiber segments.<sup>71</sup>

Infrared spectroscopy is also potentially useful for following protein assembly and disassembly. Insulin, which is key for the glucose cycle, binds to the insulin receptor in its monomeric form. However, in the body the hormone is stored as zinc-bound hexamers each of which consists of three homodimers. For human WT insulin the stabilization of the dimer with respect to two separated monomers has been determined experimentally ( $\Delta G = -7.2$  kcal/mol)<sup>72</sup> and all-atom simulations in explicit solvent confirm these measurements ( $\Delta G$  ranging from  $-8.4$  to  $-11.9$  kcal/mol from free energy simulations and  $-12.4$  kcal/mol along the minimum energy path).<sup>73-75</sup> However, for pharmaceutical applications modified insulins have been used and are being designed for which dimerization free energies are not available.

Experimental studies have provided insights about parts of the dissociation pathway between the dimer and the separated monomer. Two-dimensional IR studies in the amide-I region coupled with  $T$ -jump for the dimer indicate that monomers within the dimer rearrange on the 5 to 150  $\mu$ s time scale.<sup>76,77</sup> Between 250 and 1000  $\mu$ s the  $\beta$ -sheet structure at the dimer interface is lost. Complementary to this, time-resolved X-ray scattering studies reported the population of two intermediate dimer states,  $D_1$  and  $D_2$ , on the 310 ns and 900 ns time scale.<sup>78</sup> Although these studies are valuable from a spectroscopic perspective, they only provide limited structural information.

Computational infrared spectroscopy based on MD simulations provides a means to link structural dynamics and spectroscopy. For insulin monomer and dimer, MD simulations using validated multipolar force fields have shown that amide-I spectroscopy at the dimerization interface - involving residues PheB24, PheB25, and TyrB26 - depends on the aggregation

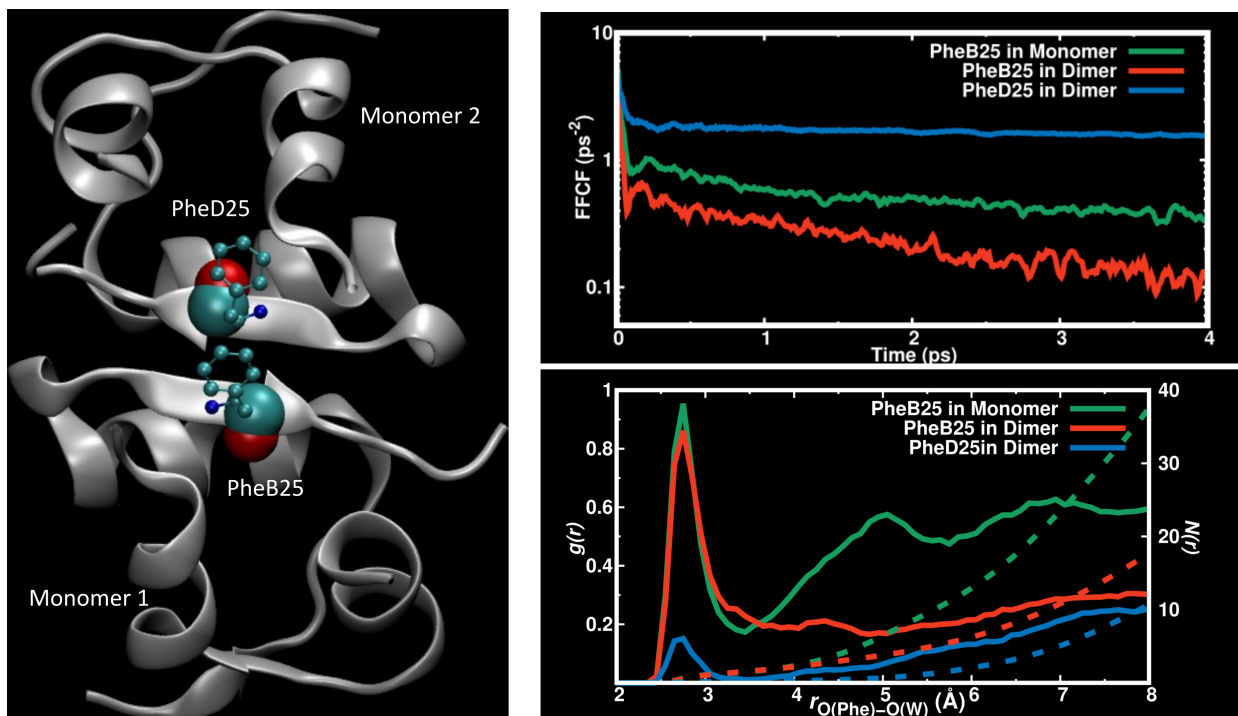


Figure 1: Structural dynamics involving the PheB25 residue in monomeric and dimeric insulin. Left panel: The structure of the insulin dimer with residues PheB25 and PheD25 as highlighted by the blue spheres and the  $-\text{CO}$  group as van der Waals spheres. Upper right panel: the frequency fluctuation correlation function for PheB25 in the monomer (green), and for PheB25 and PheD25 in the dimer (red and blue). Lower right panel: the hydration of the  $-\text{CO}$  group for PheB25 in the monomer (green solid line), and for PheB25 and PheD25 in the dimer (red and blue solid lines) together with the total number of water molecules  $N(r)$  as dashed lines with the same color code.

state,<sup>79</sup> see Figure 1 for Phe25 as an example. In other words, the IR response of the -CO reporters for residues B24 to B26 from the isolated monomer in solution differs from that of the two monomers in the dimer. In addition, the position of the maxima in the IR absorption and the dynamics of the symmetry-equivalent residues [B24,D24], [B25,D25], and [B26,D26] is not identical. This suggests that the two monomers in the dimer are dynamically not identical on the time scale of the simulations. Figure 1 demonstrates that the FFCF for PheB25 in the monomer differs from that of PheB25 and PheD25 that also differ from one another in the dimer. These findings are also consistent with X-ray experiments which found the two monomers to be not exactly symmetric.<sup>80</sup> In this context it is of interest to note that “..[the] ability of the insulin molecule to adopt different conformations may be an important factor in the expression of its biological activity..”.<sup>81</sup> Hence, the dynamical asymmetry found in the present work for WT and mutant insulin dimers may have functional implications. Overall, these findings also support the conclusions from recent MD simulations which report that early along the pathways between insulin dimer and two separate monomers the two monomers behave asymmetrically.<sup>82</sup>

The spectroscopy and reaction dynamics of photodissociated CO and NO in Myoglobin (Mb) has been investigated intensely over the past  $\sim 50$  years. For the present discussion, the infrared spectroscopy and rebinding dynamics (see next section) is of primary interest. Experimentally, the IR spectrum of the photodissociated CO ligand was found to exhibit a split spectrum with two peaks separated by  $\sim 10 \text{ cm}^{-1}$  which was associated with two conformational substates. Despite some early efforts,<sup>83,84</sup> the assignment of these two states was unclear until simulations with sufficiently detailed electrostatic models for the free ligand were used.<sup>85,86</sup> Together with subsequent mutation studies<sup>87</sup> the more red-shifted peak was associated with the Fe-OC orientation whereas the less red-shifted peak corresponds to the Fe-CO state.<sup>88</sup> Figure 2 shows the overall IR spectrum of the free CO ligand (red dashed line) together with spectra for the two suspected conformational substates (Fe-CO in green;

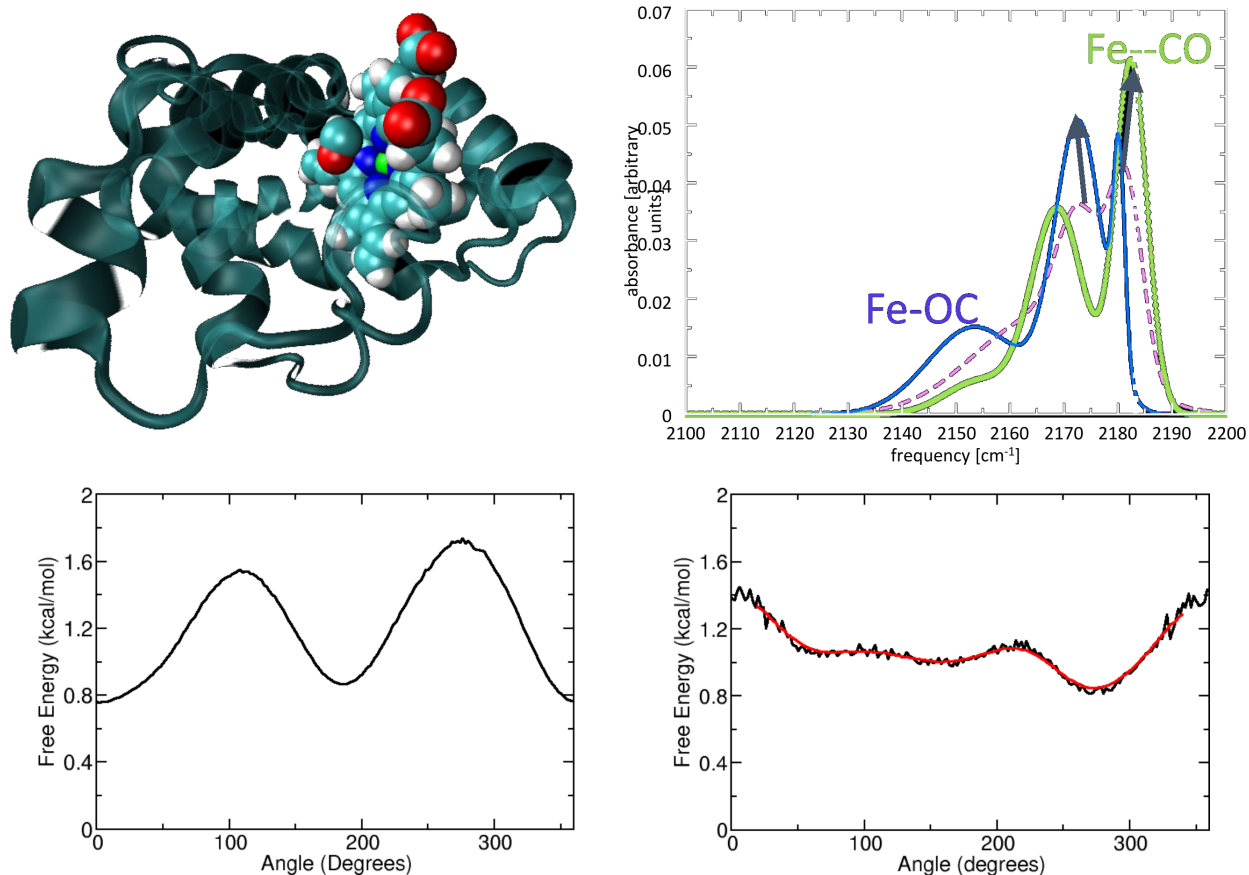


Figure 2: The infrared spectroscopy of photodissociated CO in myoglobin (Mb). Upper left panel: Structure of the protein with heme and CO as van der Waals spheres and the heme-Fe as a green sphere. Upper right panel the infrared spectrum from a 2 ns simulation using a multipolar representation for the CO molecule. The dashed line is for the full trajectory whereas the blue and green solid lines are for the parts of the trajectory during which the Fe-OC and Fe-CO are sampled predominantly. Lower left panel: the free energy profile for the rotation between Fe-CO ( $\theta = 0$ ) and Fe-OC ( $\theta = 180^\circ$ ) from the simulation with multipoles on the CO. Lower right panel: free energy profile along  $\theta$  with a point charge model for CO. Black trace is the raw data and red trace a running average.

Fe–OC in blue). Firstly, the total spectrum agrees favourably with the experimentally reported spectrum. Secondly, the state-specific spectra suggest that although they provide an identification of the two states, while sampling one substate, e.g. Fe–CO, the spectroscopy is still sensitive to the presence of the second state, i.e. Fe–OC. The reason for this is the low isomerization barrier between the two states which is reported in the lower left panel in Figure 2. The Fe–CO state ( $\theta = 0$ ) is somewhat more stable than the Fe–OC orientation ( $\theta = 180^\circ$ ) and the two states are separated by a barrier of  $\sim 0.7$  kcal/mol, compared with the experimentally reported barrier of 0.5 kcal/mol.<sup>89</sup> The lower right panel in Figure 2 shows the free energy profile along the CO rotation angle when using a point charge model and demonstrates the superiority of a more refined interaction model based on atomic multipoles.

## Reaction Dynamics

Following chemical reactions by way of computer simulations is a challenging undertaking. Although in principle *ab initio* MD (AIMD) simulations provide an obvious route, computational feasibility and accuracy often preclude such an approach. Routine applications of full AIMD simulations for reactions are typically limited to tens or hundreds of trajectories covering 10s to 100s of picoseconds of simulation time at the semiempirical or density functional theory (DFT) level.<sup>90–92</sup>

For tri- or tetra-atomic systems the investigation of reaction dynamics at the classical or quantum nuclear dynamics level has an extensive history, dating back at least to the earliest H+H<sub>2</sub> hydrogen exchange simulations<sup>93</sup> based on a reactive London-Eyring-Polanyi-Sato (LEPS) surface.<sup>94–96</sup> One surprising finding was that such quasi-classical trajectory (QCT) simulations agree quite well with rigorous quantum simulations<sup>97</sup> despite the fact that the H+H<sub>2</sub> system is particularly susceptible to quantum effects including zero point motion and

tunneling.

With the advent of efficient, high-level electronic structure calculations the configurational space of small systems could be covered adequately by computing energies for many geometries. As a consequence, empirical PESs were largely superseded and the problem shifted to representing the computed points such that the total potential energy can be evaluated with comparable accuracy as the underlying quantum chemical calculations. Fitting full-dimensional PESs even for triatomic systems is still a formidable task and with increasing number of dimensions becomes progressively more difficult. One difficulty that is encountered and detrimental to the dynamics of the system is the presence of “holes” in the PES.<sup>98–101</sup> Holes may even develop in non-parametric, machine-learned energy functions.<sup>101,102</sup> On the other hand kernel-based representations with physically meaningful asymptotic decay for large separations are less prone for developing irregular features.<sup>10,103</sup>

Recent studies of gas-phase reaction dynamics have used machine-learned PESs based on permutationally invariant polynomials (PIPs),<sup>104</sup> PIPs using neural networks (NNs),<sup>105</sup> Gaussian Processes,<sup>106</sup> reproducing kernel Hilbert space (RKHS) representations,<sup>10,103</sup> or deep NNs such as PhysNet or DeePMD.<sup>107,108</sup> A topical application of a PIP-fitted PES to high-level electronic structure calculations (MRCI, CCSD(T), and CCSD(T)-F12)<sup>109</sup> concerned the characterization of rotational resonances in the H<sub>2</sub>CO roaming reaction.<sup>110</sup> The particular interest in this study was to provide an explanation for the origin of the experimentally observed bimodal distribution of the CO fragments following the decay of the excited H<sub>2</sub>CO reactant according to [H<sub>2</sub>CO]\* → [H+HCO]\* → [H<sub>2</sub>]\* + [CO]\*. In the second step roaming of the H-atom eventually leads to abstraction of the hydrogen from HCO to form the products. Although the QCT simulations did not quantitatively reproduce the experimentally measured rotational distributions  $P(j)$ , their bimodal structure was correctly captured. Analysis of the trajectories revealed that the low- $j$  portion of  $P(j)$  passes through a cis-like OCH...H

geometry whereas the high- $j$  trajectories rather sample a trans-like  $\text{OCH}\cdots\text{H}$  geometry. This provides a detailed understanding for the relationship between the topography of the PES, the dynamics supported by it, and how this is reflected in the experimental observables.

Another area where ML-based PESs have been extensively used is in the field of high-energy reactions such as in combustion and in hypersonics. The DeePMD NN-based PES was used to understand the combustion of methane.<sup>111</sup> From a 1 ns long simulation almost 800 reactions were recorded. In addition, the simulations discovered previously unknown reaction pathways and products. For example, cyclopropene was formed in a sequence of reactions involving  $\text{CH}_2\text{CO}+\text{CH}_3$  to form cycloprop-2-en-1-one which, after colliding with another  $\text{CH}_3$ , formed  $\text{CH}_3\text{CCH}_2$  and finally stabilized as cyclopropene after further hydrogen loss. This also highlights that atomistic simulations based on machine learned PESs can be used to discover new reactions, provided that the statistical model covers chemical space sufficiently well and provides realistic reaction energetics.

The investigation of hypersonic re-entry is a challenging endeavour on multiple length and time scales. Hypersonic flight is characterized by shock waves with temperatures up to 20000 K. The chemistry is dominated by atom+diatom reactions with the reactant molecules often in highly excited ro-vibrational states. Because the flow contains species such as N, O, NO,  $\text{N}_2$ ,  $\text{O}_2$ , CO, or CN, reaction networks are required to describe the chemical evolution of the flow. This is often based on thermal rates  $k(T)$  which can, however, not be determined experimentally for the entire temperature range required. Instead, rates can be determined from high-level PESs and corresponding QCT simulations.

This has been done for the  $[\text{NOO}]$ ,<sup>112</sup>  $[\text{NNO}]$ ,<sup>113</sup>  $[\text{CNO}]$ ,<sup>114</sup> and  $[\text{COO}]$ <sup>115</sup> systems based on full-dimensional, reactive RKHS PESs and QCT simulations. In all cases thermal reaction and vibrational relaxation rates are in good agreement with existing experiments for temper-

atures up to  $T \sim 5000$  K which allows extrapolation to higher temperatures. As an example of the additional information atomistic simulations can provide the example of non-reactive and reactive vibrational relaxation of CO in collisions with atomic oxygen is considered. For the non-reactive case, non-relaxing trajectories  $\text{O}+\text{CO}(v=1) \rightarrow \text{O}+\text{CO}(v'=1)$  collide predominantly in a T-shaped geometry and do not enter the strongly interacting region of the collision complex, see Figure 3A. This differs for vibrationally relaxing trajectories  $\text{O}+\text{CO}(v=1) \rightarrow \text{O}+\text{CO}(v'=0)$  for which all collide in a nearly-linear geometry  $\text{O}\cdots\text{CO}$  and enter the strongly interaction part of the PES in panel B.<sup>115</sup> Similar to the bimodal product state distribution of CO following the decay of  $\text{H}_2\text{CO}$ ,<sup>110</sup> particular reaction channels can be associated with sampling of specific parts of the PES.

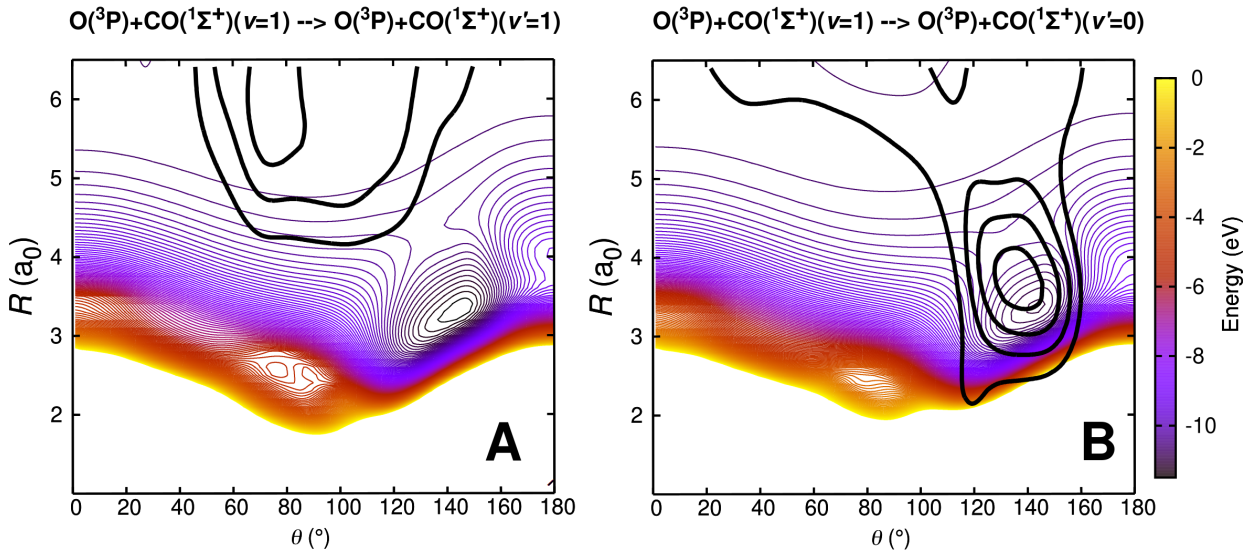


Figure 3: Vibrational relaxation for the  $\text{CO}(^1\Sigma^+; v=1)+\text{O}(^3\text{P})$  collision. The underlying PES is for the  $^3\text{A}'$  state with an equilibrium geometry for bent  $\text{CO}_2$  with  $\theta_{\text{OCO}} \sim 140^\circ$ . Panel A shows the density distribution from all non-relaxing ( $\text{O}(^3\text{P})+\text{CO}(^1\Sigma^+; v=1)\rightarrow\text{O}(^3\text{P})+\text{CO}(^1\Sigma^+; v'=1)$ ) and panel B for all relaxing ( $\text{O}(^3\text{P})+\text{CO}(^1\Sigma^+; v=1)\rightarrow\text{O}(^3\text{P})+\text{CO}(^1\Sigma^+; v'=0)$ ) trajectories.

Finally, reactive PESs have also been used for applications in atmospheric chemistry. One early example is the investigation of vibrationally induced reactivity in sulfuric acid which has been proposed based on experiments<sup>116</sup> and demonstrated in a series of atomistic simula-

tions using AIMD<sup>117</sup> or reactive MD techniques.<sup>118–120</sup> More recently, the Criegee intermediate and its decomposition to  $\text{CH}_2\text{COH}+\text{OH}$  has raised considerable interest due to both, its relevance in atmospheric processes, in particular in ozonolysis,<sup>121–125</sup> and the availability of a wealth of experimental data.<sup>126–128</sup> A first study was based on a PES fit to PIPs and used in quasiclassical trajectory (QCT) calculations. This PES was fit to  $\sim 157000$  electronic energies (a mixture of CCSD(T) and CASPT2) and covered *syn*- $\text{CH}_3\text{CHOO}$ , the transition state (TS) to vinyl hydroxyperoxide (VHP), several exit channel wells and the  $\text{OH}+\text{vinoxy}$  products. The QCT calculations were initiated at the TS separating the *syn*- $\text{CH}_3\text{CHOO}$  and VHP wells instead of the *syn* minimum. This was done owing to the long lifetime of the energized *syn*- $\text{CH}_3\text{CHOO}$  and the large computational effort needed to propagate the trajectories.

In a more recent exploration<sup>129</sup> of the full reaction pathway between *syn*- $\text{CH}_3\text{CHOO}$  and the  $\text{CH}_2\text{COH}+\text{OH}$  product a MS-ARMD-based PES surface was fit to several thousand reference energies and a PhysNet-PES was generated for  $\sim 100000$  energies, both at the MP2 level of theory. Next, an aggregate of  $\sim 10^5$  classical trajectory calculations from thermal ensembles at different temperatures of the *syn*- $\text{CH}_3\text{CHOO}$  reactant state were carried out to follow the reactive dynamics after vibrational excitation of the CH stretch with two vibrational quanta. The energy dependence of the experimentally measured rates for OH-elimination were realistically described from such a computational approach.

Reactive dynamics simulations can also be carried out in solution. One example is the  $\text{F} + \text{CD}_3\text{CN}$  abstraction reaction to form  $\text{DF}+\text{CD}_2\text{CN}$  in  $\text{CD}_3\text{CN}$  which was treated with a multi-state empirical valence bond (EVB) approach.<sup>130</sup> This work reproduced the experimentally observed<sup>131</sup> solvatochromic shift of the DF product in  $\text{CD}_3\text{CN}$  and reported that the DF product contains a significant amount of vibrational energy ( $v = 2 - 3$ ). EVB-based approaches have also been employed extensively in biomolecular simulations.<sup>132–136</sup> From

a ML perspective, RKHS-represented PESs have been used akin to QM/MM simulations for ligand rebinding reactions of ligands to proteins, in particular CO and NO to heme-containing proteins.<sup>137-139</sup>

## Concluding Remarks and Prospects

So far the focus has been on carrying out atomistic simulations with input from machine learning at the level of the energy function, its parametrization and its representation.<sup>7,140</sup> While this aspect will gain in relevance in the time to come, *analysis* of MD-generated trajectory is an equally important aspect. After all, the analysis of such trajectories provides the information to generate observables that can be compared with experiments. This comparison is the necessary step for validation of the computations with the laboratory experiments or from observations.

An early procedure for extracting progression coordinates from MD was based on a neural network and was applied to alanine dipeptide.<sup>141</sup> This work employed a genetic neural network to extract a minimal set of internal degrees of freedom to describe the  $C_{7eq} \rightarrow \alpha_R$  transition for the solvated dipeptide. For this, the committor probability was used as the target function to be optimized. For the transition in the gas phase two descriptors (two dihedral angles) were sufficient whereas for the transition in solution three coordinates were required (one dihedral, one intramolecular separation and the torque around one C-N bond). More recently, a generalization of this framework based on artificial NNs was presented.<sup>142</sup>

Machine learning was also used to determine essential internal coordinates from extended protein MD simulations.<sup>143</sup> The decision tree-based method (XGBoost)<sup>144</sup> was used to characterize metastable states of heat shock protein-35 and transitions between them and to the

open/closed transition in Lysozyme. Because the ML-based approach directly operates on a pool of candidate features (typically atom distances, valence angles, dihedral angles) the analysis provides an importance score for each of the features for a transition between two states. This differs from the more widely used principle component analysis (PCA) which only yields the linear combination of such variables. For Lysozyme analysis by XGBoost clarified that the distance  $d_{4,60}$  between residues Phe4 and Lys60 is involved in the open-to-closed transition and that the more obvious separation between residues Thr21 and Thr142 is not a suitable progression coordinate. Importantly, PCA did not find the relevance of  $d_{4,60}$  which suggests that ML-based methods can be profitably used to uncover mechanistic aspects of functional protein motions.

For chemical reactions ML-based methods were recently used to study determinants in the reaction well that do or do not lead to chemically productive (i.e. reactive) trajectories.<sup>145</sup> This study confirmed that results from machine learning confirm earlier proposals concerning the importance of electrostatic preorganization, or enzyme-stabilized “near-attack” conformations as relevant for enzymatic activity. As MD simulations provide both, coordinate and velocity trajectories it is of interest to query whether one or the other is more suitable to predict relevant degrees of freedom. It was found that both types of information can distinguish reactive from almost-reactive trajectories and that their combination performs even slightly better. It is of interest to juxtapose the insight that while still sampling the reactant well it is possible to predict whether or not a particular trajectory is likely to react with explicit sampling of reactive vs. non-reactive initial conditions.<sup>146</sup> Analysis of the minimum dynamical path for reactions in the gas phase showed that specific combinations of initial position and momenta in the reactant state lead to reactive trajectories whereas initial conditions outside this manifold do not react.

Another application of ML methods to chemical reactions is the prediction of reaction rates.

This has been done directly for rates from a library of  $\sim 40$  bimolecular reactions for which  $T$ -dependent rates from transition state theory (TST), the Eckart correction to TST, and a set of tabulated “accurate rates” from 2-dimensional calculations at 8 temperatures is available.<sup>147</sup> This data was used to learn a correction to the product of the TST-rate and the Eckart correction by using Gaussian process regression. The results for reactions not used in the learning procedure indicate that it is possible to obtain thermal rates close to those from explicit quantum simulations (using MCTDH)<sup>148</sup> or trajectory-based quantum calculations (ring polymer MD).<sup>149</sup>

An alternative procedure was followed from determining state-to-state (STS) reaction probabilities for bimolecular reactions and computing the thermal rates from the final state distributions.<sup>150</sup> From quasiclassical trajectory (QCT) simulations for the  $\text{N}(^4\text{S})+\text{NO}(^2\Pi) \rightarrow \text{O}(^3\text{P})+\text{N}_2(\text{X}^1\Sigma_g^+)$  reaction the state-to-state cross sections  $\sigma_{v,j \rightarrow v',j'}(E_t)$  as a function of the translational energy  $E_t$  were explicitly determined for 1232 initial states which amounted to  $\sim 10^8$  QCT trajectories in total compared with an estimated  $10^{15}$  QCT trajectories required for brute-force sampling of the problem. This information was used as input to train a NN together with features such as the internal energy, the vibrational and rotation energy of the diatoms, or the turning points of the diatoms.<sup>150</sup> From the NN-predicted STS cross sections the thermal rate is obtained from integrating over all  $v$ - and  $j$ - states and  $E_t$  using Monte Carlo integration. Comparison with rates directly determined from QCT simulations shows that the trained NN reaches accuracies better than 99 % over a wide temperature range ( $1000 \leq T \leq 20000$ ) K. A very recent generalization was concerned with learning entire product state distributions for specific reactant states (state-to-distribution model; STD).<sup>151</sup> The performance of this model is equally good as the STS model but at considerably reduced computational cost. At the most coarse-grained level, NNs can also be used to learn product state distributions from distributions of initial reactant states from which again thermal rates can be determined.<sup>152</sup>

It is also possible to apply machine learning methods to spectroscopy. One recent application is to learn spectroscopic maps that are used for 1- and 2-dimensional infrared spectroscopy.<sup>153</sup> Gaussian regression was used for a  $\Delta$ -learning-based approach to improve an initial set of transition frequencies and dipole derivatives for the water-OH stretch. Compared with a conventional, parametrized spectroscopic map the machine learned model reduced the errors for the transition frequencies and the dipole derivatives by a factor of  $\sim 2$ . The additional computational overhead of the ML-based model compared with a conventional spectroscopic map is a factor of  $\sim 10^4$ .

Exploration of reaction mechanisms is another future application of ML-based techniques. This has, for example, been noted when investigating the combustion of methane.<sup>111</sup> Atmospheric and interstellar chemistry are further fields for which this can become relevant. For example, considering the  $O(^1D)+CO(^1\Sigma^+)$  reaction on amorphous solid water (ASW).<sup>154,155</sup> Using a RKHS-based reactive PES for the recombination reaction it was not only demonstrated that  $CO_2$  can form and stabilize on ASW. Consistent with earlier experiments<sup>156</sup> the simulations also show that the COO isomer can form and stabilize, see Figure 4. Other recent applications of ML-based energy functions to interstellar chemistry concern the diffusion of atomic oxygen<sup>157</sup> and nitrogen<sup>158</sup> and the formation of  $O_2$  on ASW.<sup>159,160</sup>

Atomistic simulations will continue to benefit from synergies with machine learning technology. This includes both, the implementation and technical advances of ML. From a computational perspective it is desirable to fully integrate ML PESs into existing MD codes for efficiency reasons and not to use a ML PES as an external energy function akin to QM/MM calculations. From a technological perspective, rigorous application of transfer- or  $\Delta$ -learning approaches offer much scope to go beyond DFT-based PESs in an efficient manner. First steps in this direction have been undertaken.<sup>161,162</sup>

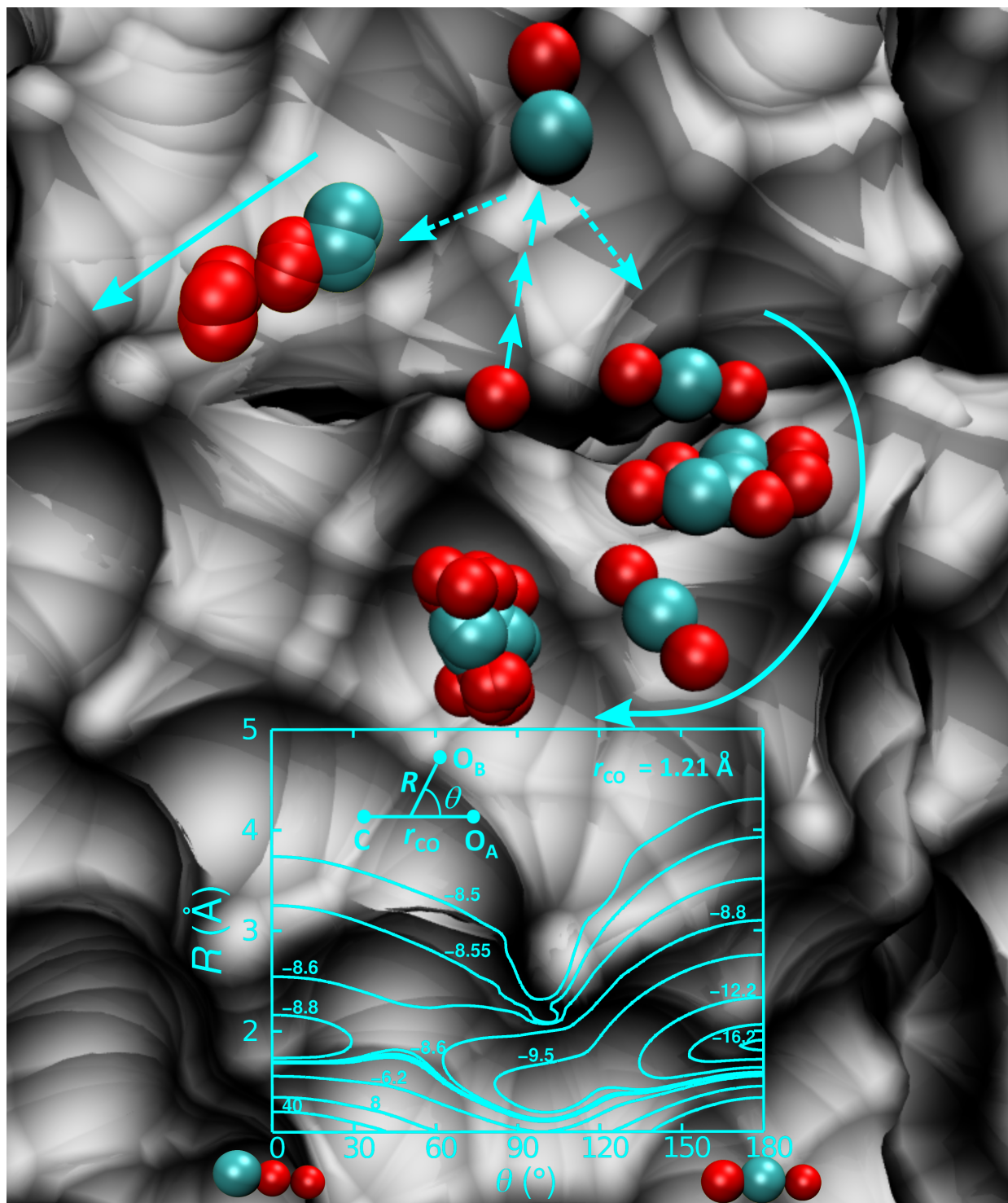


Figure 4: CO+O recombination on amorphous solid water. The ground state PES supports both, the global OCO and the local COO minimum energy structure. Both are formed and stabilized from reactive MD simulations using the RKHS interpolated MRCI+Q/aug-cc-pVTZ reference energies.

Another imminent improvement is the realistic description of long range interactions. Most machine-learned PES are restricted to exploration of the energetics around well-defined reference (minimum energy) structures or for small reference systems using local representations. However, for chemical reactions or systems in the condensed phase the long range part of the intermolecular interaction is essential and determining reference structures for input into ML-based models becomes increasingly costly. This was recently addressed within the DeepMD framework by using Wannier functions centered on the atoms.<sup>163</sup> Alternatively, it may also be possible to combine a short-ranged ML-PES with explicit long range representations based on multipoles as has been done for ionic complexes.<sup>164</sup> On the other hand, with a suitable high-level implementation machine learned PESs from reference calculations in the gas phase may already be used in a QM/MM fashion in MD simulations. Such ML/MM MD simulations provide considerable speedup compared with conventional QM/MM simulations for sufficiently high levels of the QM reference. Combined with transfer learning techniques this will allow treatment of the solute at the correlated level of theory (such as MP2 or even CCSD(T)). Here it is important to stress that the computational cost for evaluating an ML PES is always the same, irrespective of the level of theory it was trained on. The computational cost for the different levels of theory used for the reference calculations arises for the reference calculations which, however, can be alleviated due to a) the massively parallel fashion in which this step can be carried out and b) the fact that TL can considerably reduce the number of high-level calculations that needs to be carried out.

In conclusion, with the ever increased computer power available, atomistic simulations combined with tools from ML have a bright and exciting future for exploring functional aspects of chemical systems. This concerns in particular, but not exclusively, systems for which state-of-the art experiments are available and can be carried out. An MD/ML-based approach can also be used for prediction of spectroscopic responses - e.g. upon protein mutation -

or reaction pathway and product exploration. This requires computationally efficient implementations and reference calculations at sufficiently high level of theory, both of which are becoming available.<sup>162,165–167</sup>

## Acknowledgement

This work was supported by the Swiss National Science Foundation grants 200021-117810, 200020-188724, the NCCR MUST, and the University of Basel.

## Author Biography

**Markus Meuwly** studied Physics at the University of Basel and completed his PhD in Physical Chemistry working with Prof. J. P. Maier. After postdocs with Prof. J. Hutson (Durham) and Prof. M. Karplus (Strasbourg and Harvard) as a Swiss National Science Foundation Postdoctoral Scholar he started as a Förderprofessor at the University of Basel in 2002 where he is Full Professor of Physical and Computational Chemistry. He also holds a visiting professorship at Brown University, Providence, RI. His scientific interests range from accurate intermolecular interactions based on multipolar, kernel- and neural network-based representations to applications of quantitative molecular simulations for cold (interstellar) and hot (hypersonics) environments and the investigation of the spectroscopy and reactive dynamics in proteins and in the condensed phase.

## References

- (1) Zwanzig, R. Time-correlation functions and transport coefficients in statistical mechanics. *Annu. Rev. Phys. Chem.* **1965**, *16*, 67–102.
- (2) Gordon, R. *Advances in Magnetic and Optical Resonance*; Elsevier, 1968; Vol. 3; pp 1–42.
- (3) Cui, Q. Perspective: Quantum mechanical methods in biochemistry and biophysics. *J. Chem. Phys.* **2016**, *145*, 140901.
- (4) Cui, Q.; Pal, T.; Xie, L. Biomolecular QM/MM Simulations: What Are Some of the "Burning Issues"? *J. Phys. Chem. B* **2021**, *125*, 689–702.
- (5) Rupp, M.; Tkatchenko, A.; Müller, K.-R.; Von Lilienfeld, O. A. Fast and accurate modeling of molecular atomization energies with machine learning. *Phys. Rev. Lett.* **2012**, *108*, 058301.
- (6) Vapnik, V. N. *Statistical Learning Theory*; Wiley-Interscience, 1998.
- (7) Unke, O. T.; Chmiela, S.; Sauceda, H. E.; Gastegger, M.; Poltavsky, I.; Schütt, K. T.; Tkatchenko, A.; Müller, K.-R. Machine learning force fields. *Chem. Rev.* **2021**, *121*, 10142–10186.
- (8) Manzhos, S.; Carrington Jr, T. Neural network potential energy surfaces for small molecules and reactions. *Chem. Rev.* **2021**, *121*, 10187–10217.
- (9) Meuwly, M. Machine Learning for Chemical Reactions. *Chem. Rev.* **2021**, *121*, 10218–10239.
- (10) Ho, T.-S.; Rabitz, H. A general method for constructing multidimensional molecular potential energy surfaces from ab initio calculations. *J. Chem. Phys.* **1996**, *104*, 2584.

- (11) Hollebeek, T.; Ho, T.-S.; Rabitz, H. Constructing multidimensional molecular potential energy surfaces from ab initio data. *Annu. Rev. Phys. Chem.* **1999**, *50*, 537–570.
- (12) Meuwly, M.; Hutson, J. The potential energy surface and near-dissociation states of He-H<sub>2</sub><sup>+</sup>. *J. Chem. Phys.* **1999**, *110*, 3418–3427.
- (13) Aronszajn, N. Theory of Reproducing Kernels. *Trans. Amer. Math. Soc.* **1950**, *68*, 337–404.
- (14) Zwier, T. S. Laser probes of conformational isomerization in flexible molecules and complexes. *J. Phys. Chem. A* **2006**, *110*, 4133–4150.
- (15) Rizzo, T. R.; Stearns, J. A.; Boyarkin, O. V. Spectroscopic studies of cold, gas-phase biomolecular ions. *Int. Rev. Phys. Chem.* **2009**, *28*, 481–515.
- (16) Amadei, A.; Daidone, I.; Di Nola, A.; Aschi, M. Theoretical-computational modelling of infrared spectra in peptides and proteins: a new frontier for combined theoretical-experimental investigations. *Curr. Op. Struct. Biol.* **2010**, *20*, 155–161.
- (17) Feng, C. J.; Dhayalan, B.; Tokmakoff, A. Refinement of Peptide Conformational Ensembles by 2D IR Spectroscopy: Application to Ala-Ala-Ala. *Biophys. J.* **2018**, *114*, 2820–2832.
- (18) Mondal, P.; Cazade, P.-A.; Das, A. K.; Bereau, T.; Meuwly, M. Multipolar Force Fields for Amide-I Spectroscopy from Conformational Dynamics of the Alanine Trimer. *J. Phys. Chem. B* **2021**, *125*, 10928–10938.
- (19) Headrick, J. M.; Diken, E. G.; Walters, R. S.; Hammer, N. I.; Christie, R. A.; Cui, J.; Myshakin, E. M.; Duncan, M. A.; Johnson, M. A.; Jordan, K. D. Spectral signatures of hydrated proton vibrations in water clusters. *Science* **2005**, *308*, 1765–1769.
- (20) Chang, H.-C.; Wu, C.-C.; Kuo, J.-L. Recent advances in understanding the structures of medium-sized protonated water clusters. *Int. Rev. Phys. Chem.* **2005**, *24*, 553–578.

- (21) Zeng, H. J.; Johnson, M. A. Demystifying the Diffuse Vibrational Spectrum of Aqueous Protons Through Cold Cluster Spectroscopy. *Annu. Rev. Phys. Chem.* **2021**, *72*, 667–691.
- (22) Baquero, E. E.; James, W. H.; Choi, S. H.; Gellman, S. H.; Zwier, T. S. Single-conformation ultraviolet and infrared spectroscopy of model synthetic foldamers:  $\beta$ -peptides Ac- $\beta$ 3-hPhe-NHMe and Ac- $\beta$ 3-hTyr-NHMe. *J. Am. Chem. Soc.* **2008**, *130*, 4784–4794.
- (23) Yu, Q.; Bowman, J. M. Communication: VSCF/VCI vibrational spectroscopy of  $\text{H}_7\text{O}_3^+$  and  $\text{H}_9\text{O}_4^+$  using high-level, many-body potential energy surface and dipole moment surfaces. *J. Chem. Phys.* **2017**, *146*, 121102.
- (24) Yu, Q.; Bowman, J. M. High-level quantum calculations of the IR spectra of the Eigen, Zundel, and Ring isomers of  $\text{H}^+(\text{H}_2\text{O})_4$  find a single match to experiment. *J. Am. Chem. Soc.* **2017**, *139*, 10984–10987.
- (25) Åqvist, J.; Kolmodin, K.; Florian, J.; Warshel, A. Mechanistic alternatives in phosphate monoester hydrolysis: what conclusions can be drawn from available experimental data? *Chem. & Biol.* **1999**, *6*, R71–R80.
- (26) Klähn, M.; Rosta, E.; Warshel, A. On the mechanism of hydrolysis of phosphate monoesters dianions in solutions and proteins. *J. Am. Chem. Soc.* **2006**, *128*, 15310–15323.
- (27) Duarte, F.; Åqvist, J.; Williams, N. H.; Kamerlin, S. C. Resolving apparent conflicts between theoretical and experimental models of phosphate monoester hydrolysis. *J. Am. Chem. Soc.* **2015**, *137*, 1081–1093.
- (28) Menshutkin, N. Über die Affinitätskoeffizienten der Alkylhaloide und der Amine. *Zeitschrift für Phys. Chemie* **1890**, *6*, 41–57.

- (29) Allfrey, V. G.; Faulkner, R.; Mirsky, A. Acetylation and Methylation of Histones and Their Possible Role in the Regulation of RNA Synthesis. *Proc. Natl. Acad. Sci.* **1964**, *51*, 786.
- (30) Schubert, H. L.; Blumenthal, R. M.; Cheng, X. Many Paths to Methyltransfer: A Chronicle of Convergence. *Trends Biochem. Sci.* **2003**, *28*, 329–335.
- (31) Castejon, H.; Wiberg, K. B. Solvent Effects on Methyl Transfer Reactions. 1. The Menshutkin Reaction. *J. Am. Chem. Soc.* **1999**, *121*, 2139–2146.
- (32) Castejon, H.; Wiberg, K. B.; Sklenak, S.; Hinz, W. Solvent Effects on Methyl Transfer Reactions. 2. The Reaction of Amines with Trimethylsulfonium Salts. *J. Am. Chem. Soc.* **2001**, *123*, 6092–6097.
- (33) Turan, H. T.; Brickel, S.; Meuwly, M. Solvent Effects on the Menshutkin Reaction. *arXiv preprint arXiv:2111.05244* **2021**,
- (34) Houk, K. N.; González, J.; Li, Y. *Acc. Chem. Res.* **1995**, *28*, 81.
- (35) Domingo, L. R. *J. Chil. Chem. Soc.* **2014**, *2615*, 59.
- (36) Rivero, U.; Unke, O. T.; Meuwly, M.; Willitsch, S. Reactive atomistic simulations of Diels-Alder reactions: The importance of molecular rotations. *J. Chem. Phys.* **2019**, *151*, 104301.
- (37) Rivero, U.; Turan, H. T.; Meuwly, M.; Willitsch, S. Reactive atomistic simulations of Diels-Alder-type reactions: conformational and dynamic effects in the polar cycloaddition of 2, 3-dibromobutadiene radical ions with maleic anhydride. *Mol. Phys.* **2021**, *119*, e1825852.
- (38) Bowman, J. M.; Shepler, B. C. Roaming radicals. *Annu. Rev. Phys. Chem.* **2011**, *62*, 531–553.

- (39) Yanai, T.; Taketsugu, T.; Hirao, K. Theoretical study of bifurcating reaction paths. *J. Chem. Phys.* **1997**, *107*, 1137–1146.
- (40) Nienhaus, K.; Lutz, S.; Meuwly, M.; Nienhaus, G. U. Reaction-pathway selection in the structural dynamics of a heme protein. *Chem. Eur. J.* **2013**, *19*, 3558–3562.
- (41) Carpenter, B. K.; Harvey, J. N.; Glowacki, D. R. Prediction of enhanced solvent-induced enantioselectivity for a ring opening with a bifurcating reaction path. *Phys. Chem. Chem. Phys.* **2015**, *17*, 8372–8381.
- (42) Oomens, J.; Sartakov, B. G.; Meijer, G.; Von Helden, G. Gas-phase infrared multiple photon dissociation spectroscopy of mass-selected molecular ions. *Int. J. Mass. Spec.* **2006**, *254*, 1–19.
- (43) Wolk, A. B.; Leavitt, C. M.; Garand, E.; Johnson, M. A. Cryogenic ion chemistry and spectroscopy. *Acc. Chem. Res.* **2014**, *47*, 202–210.
- (44) Zanni, M. T.; Hochstrasser, R. M. Two-dimensional infrared spectroscopy: a promising new method for the time resolution of structures. *Curr. Op. Struct. Biol.* **2001**, *11*, 516–522.
- (45) Herbst, J.; Heyne, K.; Diller, R. Femtosecond infrared spectroscopy of bacteriorhodopsin chromophore isomerization. *Science* **2002**, *297*, 822–825.
- (46) Schotte, F.; Lim, M.; Jackson, T. A.; Smirnov, A. V.; Soman, J.; Olson, J. S.; Phillips, G. N.; Wulff, M.; Anfinrud, P. A. Watching a protein as it functions with 150-ps time-resolved x-ray crystallography. *Science* **2003**, *300*, 1944–1947.
- (47) Decatur, S. M. Elucidation of residue-level structure and dynamics of polypeptides via isotope-edited infrared spectroscopy. *Acc. Chem. Res.* **2006**, *39*, 169–175.
- (48) Zheng, J.; Kwak, K.; Fayer, M. Ultrafast 2D IR vibrational echo spectroscopy. *Acc. Chem. Res.* **2007**, *40*, 75–83.

- (49) Kim, Y. S.; Hochstrasser, R. M. Applications of 2D IR spectroscopy to peptides, proteins, and hydrogen-bond dynamics. *J. Phys. Chem. B* **2009**, *113*, 8231–8251.
- (50) Suydam, I. T.; Snow, C. D.; Pande, V. S.; Boxer, S. G. Electric fields at the active site of an enzyme: Direct comparison of experiment with theory. *Science* **2006**, *313*, 200–204.
- (51) Mondal, P.; Meuwly, M. Vibrational Stark spectroscopy for assessing ligand-binding strengths in a protein. *Phys. Chem. Chem. Phys.* **2017**, *19*, 16131–16143.
- (52) Bloem, R.; Koziol, K.; Waldauer, S. A.; Buchli, B.; Walser, R.; Samatanga, B.; Jelezarov, I.; Hamm, P. Ligand Binding Studied by 2D IR Spectroscopy Using the Azido-homoalanine Label. *J. Phys. Chem. B* **2012**, *116*, 13705–13712.
- (53) Zanobini, C.; Bozovic, O.; Jankovic, B.; Koziol, K. L.; Johnson, P. J. M.; Hamm, P.; Gulzar, A.; Wolf, S.; Stock, G. Azidohomoalanine: A Minimally Invasive, Versatile, and Sensitive Infrared Label in Proteins To Study Ligand Binding. *J. Phys. Chem. B* **2018**, *122*, 10118–10125.
- (54) Kiick, K.; Saxon, E.; Tirrell, D.; Bertozzi, C. Incorporation of azides into recombinant proteins for chemoselective modification by the Staudinger ligation. *Proc. Natl. Acad. Sci.* **2002**, *99*, 19–24.
- (55) Salehi, S. M.; Meuwly, M. Site-selective dynamics of azidolysosome. *J. Chem. Phys.* **2021**, *154*, 165101.
- (56) Ho, T.-S.; Rabitz, H. A General Method for Constructing Multidimensional Molecular Potential Energy Surfaces from Ab Initio Calculations. *J. Chem. Phys.* **1996**, *104*, 2584–2597.
- (57) Unke, O. T.; Meuwly, M. Toolkit for the Construction of Reproducing Kernel-Based

- Representations of Data: Application to Multidimensional Potential Energy Surfaces. *J. Chem. Inf. Model.* **2017**, *57*, 1923–1931.
- (58) Schwilk, M.; Ma, Q.; Köppl, C.; Werner, H.-J. Scalable Electron Correlation Methods. 3. Efficient and Accurate Parallel Local Coupled Cluster with Pair Natural Orbitals (PNO-LCCSD). *J. Chem. Theor. Comp.* **2017**, *13*, 3650–3675.
- (59) Ma, Q.; Schwilk, M.; Köppl, C.; Werner, H.-J. Scalable electron correlation methods. 4. Parallel explicitly correlated local coupled cluster with pair natural orbitals (PNO-LCCSD-F12). *J. Chem. Theor. Comp.* **2017**, *13*, 4871–4896.
- (60) Woutersen, S.; Hamm, P. Structure Determination of Trialanine in Water Using Polarization Sensitive Two-Dimensional Vibrational Spectroscopy. *J. Phys. Chem. B* **2000**, *104*, 11316–11320.
- (61) Woutersen, S.; Pfister, R.; Hamm, P.; Mu, Y.; Kosov, D. S.; Stock, G. Peptide Conformational Heterogeneity Revealed from Nonlinear Vibrational Spectroscopy and Molecular-Dynamics Simulations. *J. Chem. Phys.* **2002**, *117*, 6833–6840.
- (62) Woutersen, S.; Mu, Y.; Stock, G.; Hamm, P. Subpicosecond conformational dynamics of small peptides probed by two-dimensional vibrational spectroscopy. *Proc. Natl. Acad. Sci.* **2001**, *98*, 11254–11258.
- (63) Schweitzer-Stenner, Q. H. R.; Eker, F.; Griebenov, K. Dihedral Angles of Trialanine in D<sub>2</sub>O Determined by Combining FTIR and Polarized Visible Raman Spectroscopy. *J. Am. Chem. Soc.* **2001**, *123*, 9628–9633.
- (64) Woutersen, S.; Hamm, P. Isotope-edited two-dimensional vibrational spectroscopy of trialanine in aqueous solution. *J. Chem. Phys.* **2001**, *114*, 2727.
- (65) Mu, Y.; Stock, G. Conformational Dynamics of Trialanine in Water : A Molecular Dynamical Study. *J. Phys. Chem. B* **2002**, *106*, 5294–5301.

- (66) Graf, J.; Nguyen, P. H.; Schwalbe, H. Structure and dynamics of the homologous series of alanine peptides: a joint molecular dynamics/NMR study. *J. Am. Chem. Soc.* **2007**, *129*, 1179–1189.
- (67) Gorbunov, R. D.; Nguyen, P. H.; Kobus, M.; Stock, G. Quantum-classical description of the amide I vibrational spectrum of trialanine. *J. Chem. Phys.* **2007**, *126*, 054509–054516.
- (68) Oh, K. I.; Lee, K. K.; Cho, M. Circular dichroism eigen spectra of polyproline II and  $\beta$ -strand conformers of trialanine in water: singular value decomposition analysis. *Chirality* **2010**, *22*, E186–E201.
- (69) Xiao, X.; Kallenbach, N.; Zhang, Y. Peptide conformation analysis using an integrated Bayesian approach. *J. Chem. Theo. Comput.* **2014**, *10*, 4152–4159.
- (70) Moran, S. D.; Zanni, M. T. How to get insight into amyloid structure and formation from infrared spectroscopy. *J. Phys. Chem. Lett.* **2014**, *5*, 1984–1993.
- (71) Buchanan, L. E.; Carr, J. K.; Fluitt, A. M.; Hoganson, A. J.; Moran, S. D.; de Pablo, J. J.; Skinner, J. L.; Zanni, M. T. Structural motif of polyglutamine amyloid fibrils discerned with mixed-isotope infrared spectroscopy. *Proc. Natl. Acad. Sci.* **2014**, *111*, 5796–5801.
- (72) Strazza, S.; Hunter, R.; Walker, E.; Darnall, D. W. The thermodynamics of bovine and porcine insulin and proinsulin association determined by concentration difference spectroscopy. *Arch. Biochem. Biophys.* **1985**, *238*, 30–42.
- (73) Zoete, V.; Meuwly, M.; Karplus, M. Study of the insulin dimerization: binding free energy calculations and per-residue free energy decomposition. *Prot. Struc. Func. Bioinf.* **2005**, *61*, 79–93.

- (74) Raghunathan, S.; El Hage, K.; Desmond, J. L.; Zhang, L.; Meuwly, M. The role of water in the stability of wild-type and mutant insulin dimers. *J. Phys. Chem. B* **2018**, *122*, 7038–7048.
- (75) Banerjee, P.; Mondal, S.; Bagchi, B. Effect of ethanol on insulin dimer dissociation. *J. Chem. Phys.* **2019**, *150*, 084902.
- (76) Ganim, Z.; Jones, K. C.; Tokmakoff, A. Insulin dimer dissociation and unfolding revealed by amide I two-dimensional infrared spectroscopy. *Phys. Chem. Chem. Phys.* **2010**, *12*, 3579–3588.
- (77) Zhang, X.-X.; Jones, K. C.; Fitzpatrick, A.; Peng, C. S.; Feng, C.-J.; Baiz, C. R.; Tokmakoff, A. Studying protein–protein binding through T-jump induced dissociation: Transient 2D IR spectroscopy of insulin dimer. *J. Phys. Chem. B* **2016**, *120*, 5134–5145.
- (78) Rimmerman, D.; Leshchev, D.; Hsu, D. J.; Hong, J.; Kosheleva, I.; Chen, L. X. Direct observation of insulin association dynamics with time-resolved X-ray scattering. *J. Phys. Chem. Lett.* **2017**, *8*, 4413–4418.
- (79) Salehi, S. M.; Koner, D.; Meuwly, M. Dynamics and infrared spectroscopy of monomeric and dimeric wild type and mutant insulin. *J. Phys. Chem. B* **2020**, *124*, 11882–11894.
- (80) Baker, E.; Blundell, T.; Cutfield, J.; Cutfield, S.; Dodson, E.; Dodson, G.; Hodgkin, D. M.; Hubbard, R.; Isaacs, N.; Reynolds, C. The structure of 2Zn pig insulin crystals at 1.5 Å resolution. *Phil. Trans. R. Soc. Lond. B Biol.* **1988**, *319*, 369–456.
- (81) Dodson, E.; Hodgkin, D.; Reynolds, C.; Dodson, G. Structural Relationships in the 2-Zinc insulin Hexamer. *Can. J. Biochem.* **1979**, *57*, 469–479.

- (82) Antoszewski, A.; Feng, C.-J.; Vani, B. P.; Thiede, E. H.; Hong, L.; Weare, J.; Tokmakoff, A.; Dinner, A. R. Insulin dissociates by diverse mechanisms of coupled unfolding and unbinding. *J. Phys. Chem. B* **2020**, *124*, 5571–5587.
- (83) Meller, J.; Elber, R. Computer simulations of carbon monoxide photodissociation in myoglobin: structural interpretation of the B states. *Biophys. J.* **1998**, *74*, 789–802.
- (84) Anselmi, M.; Aschi, M.; Di Nola, A.; Amadei, A. Theoretical characterization of carbon monoxide vibrational spectrum in sperm whale myoglobin distal pocket. *Biophys. J.* **2007**, *92*, 3442–3447.
- (85) Nutt, D. R.; Meuwly, M. Theoretical investigation of infrared spectra and pocket dynamics of photodissociated carbonmonoxy myoglobin. *Biophys. J.* **2003**, *85*, 3612–3623.
- (86) Plattner, N.; Meuwly, M. The role of higher CO-multipole moments in understanding the dynamics of photodissociated carbonmonoxide in myoglobin. *Biophys. J.* **2008**, *94*, 2505–2515.
- (87) Nienhaus, K.; Olson, J. S.; Franzen, S.; Nienhaus, G. U. The origin of stark splitting in the initial photoproduct state of MbCO. *J. Am. Chem. Soc.* **2005**, *127*, 40–41.
- (88) Meuwly, M. On the Influence of the Local Environment on the CO Stretching Frequencies in Native Myoglobin: Assignment of the B-States in MbCO. *Chem. Phys. Chem.* **2006**, *7*, 2061–2063.
- (89) Kriegl, J. M.; Nienhaus, K.; Deng, P.; Fuchs, J.; Nienhaus, G. U. Ligand dynamics in a protein internal cavity. *Proc. Natl. Acad. Sci.* **2003**, *100*, 7069–7074.
- (90) Meuwly, M.; Karplus, M. Simulation of proton transfer along ammonia wires: An "ab initio" and semiempirical density functional comparison of potentials and classical molecular dynamics. *J. Chem. Phys.* **2002**, *116*, 2572–2585.

- (91) Miller, Y.; Gerber, R. B. Dynamics of Vibrational Overtone Excitations of  $\text{H}_2\text{SO}_4$ ,  $\text{H}_2\text{SO}_4\text{-H}_2\text{O}$ : Hydrogen- Hopping and Photodissociation Processes. *J. Am. Chem. Soc.* **2006**, *128*, 9594–9595.
- (92) Hänninen, V.; Murdachaew, G.; Nathanson, G. M.; Gerber, R. B.; Halonen, L. Ab initio molecular dynamics studies of formic acid dimer colliding with liquid water. *Phys. Chem. Chem. Phys.* **2018**, *20*, 23717–23725.
- (93) Karplus, M.; Sharma, R. D.; Porter, R. N. Dynamics of Reactive Collisions -  $\text{H} + \text{H}_2$  Exchange Reaction. *J. Chem. Phys.* **1964**, *40*, 2033–2034.
- (94) London, F. Quantum mechanical interpretation of the process of activation. *Z. Elektrochem.* **1929**, *35*, 552–555.
- (95) Eyring, H.; Polanyi, M. Concerning simple gas reactions. *Z. Phys. Chem. Abt. B* **1931**, *12*, 279–311.
- (96) Sato, S. Potential energy surface of the system of three atoms. *J. Chem. Phys.* **1955**, *23*, 2465–2466.
- (97) Schatz, G.; Kuppermann, A. Quantum-mechanical reactive scattering for 3-dimensional atom plus diatom systems .2. Accurate cross-sections for  $\text{H}+\text{H}_2$ . *J. Chem. Phys.* **1976**, *65*, 4668–4692.
- (98) Fortenberry, R. C.; Yu, Q.; Mancini, J. S.; Bowman, J. M.; Lee, T. J.; Crawford, T. D.; Klemperer, W. F.; Francisco, J. S. Communication: Spectroscopic consequences of proton delocalization in  $\text{OCHCO}^+$ . *J. Chem. Phys.* **2015**, *143*.
- (99) Pandey, A.; Poirier, B. Using phase-space Gaussians to compute the vibrational states of  $\text{OCHCO}^+$ . *J. Chem. Phys.* **2019**, *151*, 014114.
- (100) Pandey, A.; Poirier, B. Plumbing potentials for molecules with up to tens of atoms:

- how to find saddle points and fix leaky holes. *J. Phys. Chem. Lett.* **2020**, *11*, 6468–6474.
- (101) Li, J.; Qu, C.; Bowman, J. M. Diffusion Monte Carlo with fictitious masses finds holes in potential energy surfaces. *Mol. Phys.* **2021**, *119*, e1976426.
- (102) Stöhr, M.; Medrano Sandonas, L.; Tkatchenko, A. Accurate many-body repulsive potentials for density-functional tight binding from deep tensor neural networks. *J. Phys. Chem. Lett.* **2020**, *11*, 6835–6843.
- (103) Unke, O. T.; Meuwly, M. Toolkit for the Construction of Reproducing Kernel-Based Representations of Data: Application to Multidimensional Potential Energy Surfaces. *J. Chem. Inf. Model* **2017**, *57*, 1923–1931.
- (104) Braams, B. J.; Bowman, J. M. Permutationally Invariant Potential Energy Surfaces in High Dimensionality. *Int. Rev. Phys. Chem.* **2009**, *28*, 577–606.
- (105) Jiang, B.; Li, J.; Guo, H. Potential Energy Surfaces from High Fidelity Fitting of Ab Initio Points: the Permutation Invariant Polynomial-Neural Network Approach. *Int. Rev. Phys. Chem.* **2016**, *35*, 479–506.
- (106) Guan, Y.; Yang, S.; Zhang, D. H. Construction of reactive potential energy surfaces with Gaussian process regression: active data selection. *Mol. Phys.* **2018**, *116*, 823–834.
- (107) Unke, O. T.; Meuwly, M. PhysNet: A Neural Network for Predicting Energies, Forces, Dipole Moments, and Partial Charges. *J. Chem. Theor. Comp.* **2019**, *15*, 3678–3693.
- (108) Zhang, L.; Han, J.; Wang, H.; Car, R.; Weinan, E. Deep potential molecular dynamics: a scalable model with the accuracy of quantum mechanics. *Phys. Rev. Lett.* **2018**, *120*, 143001.

- (109) Wang, X.; Houston, P. L.; Bowman, J. M. A new (multi-reference configuration interaction) potential energy surface for H<sub>2</sub>CO and preliminary studies of roaming. *Philosophical Transactions of the Royal Society A: Mathematical, Physical and Engineering Sciences* **2017**, *375*, 20160194.
- (110) Quinn, M. S.; Nauta, K.; Jordan, M. J.; Bowman, J. M.; Houston, P. L.; Kable, S. H. Rotational resonances in the H<sub>2</sub>CO roaming reaction are revealed by detailed correlations. *Science* **2020**, *369*, 1592–1596.
- (111) Zeng, J.; Cao, L.; Xu, M.; Zhu, T.; Zhang, J. Z. Complex reaction processes in combustion unraveled by neural network-based molecular dynamics simulation. *Nat. Comm.* **2020**, *11*, 1–9.
- (112) San Vicente Veliz, J. C.; Koner, D.; Schwilk, M.; Bemish, R. J.; Meuwly, M. The N(<sup>4</sup>S) + O<sub>2</sub>(X<sup>3</sup>Σ<sub>g</sub><sup>-</sup>) ↔ O(<sup>3</sup>P) + NO(X<sup>2</sup>Π) Reaction: Thermal and Vibrational Relaxation Rates for the <sup>2</sup>A', <sup>4</sup>A' and <sup>2</sup>A'' States. *Phys. Chem. Chem. Phys.* **2020**, *22*, 3927–3939.
- (113) Koner, D.; Veliz, J. C. S. V.; Bemish, R. J.; Meuwly, M. Accurate Reproducing Kernel-Based Potential Energy Surfaces for the Triplet Ground States of N<sub>2</sub>O and Dynamics for the N+NO↔O+N<sub>2</sub> Reaction. *Phys. Chem. Chem. Phys.* **2020**, *22*, 18488–18498.
- (114) Koner, D.; Bemish, R. J.; Meuwly, M. The C(<sup>3</sup>P) + NO(X<sup>2</sup>Π) → O(<sup>3</sup>P) + CN(X<sup>2</sup>Σ<sup>+</sup>), N(<sup>2</sup>D)/N(<sup>4</sup>S) + CO(X<sup>1</sup>Σ<sup>+</sup>) reaction: Rates, branching ratios, and final states from 15 K to 20 000 K. *J. Chem. Phys.* **2018**, *149*, 094305.
- (115) Veliz, J. C. S. V.; Koner, D.; Schwilk, M.; Bemish, R. J.; Meuwly, M. The C (<sup>3</sup>P)+ O<sub>2</sub> (<sup>3</sup>Σ<sub>g</sub><sup>-</sup>)→ CO<sub>2</sub> ↔ CO (<sup>1</sup>Σ<sup>+</sup>)+ O (<sup>1</sup>D)/O (<sup>3</sup>P) reaction: thermal and vibrational relaxation rates from 15 K to 20000 K. *Phys. Chem. Chem. Phys.* **2021**, *23*, 11251–11263.

- (116) Vaida, V.; Kjaergaard, H. G.; Hintze, P. E.; Donaldson, D. J. Photolysis of Sulfuric Acid Vapor by Visible Solar Radiation. *Science* **2003**, *299*, 1566–1568.
- (117) Miller, Y.; Gerber, R. B. Dynamics of vibrational overtone excitations of H<sub>2</sub>SO<sub>4</sub>, H<sub>2</sub>SO<sub>4</sub>-H<sub>2</sub>O: Hydrogen-hopping and photodissociation processes. *J. Am. Chem. Soc.* **2006**, *128*, 9594–9595.
- (118) Yosa, J.; Meuwly, M. Vibrationally induced dissociation of sulfuric acid (H<sub>2</sub>SO<sub>4</sub>). *J. Phys. Chem. A* **2011**, *115*, 14350–14360.
- (119) Nagy, T.; Yosa Reyes, J.; Meuwly, M. Multisurface Adiabatic Reactive Molecular Dynamics. *J. Chem. Theor. Comp.* **2014**, *10*, 1366–1375.
- (120) Yosa Reyes, J.; Nagy, T.; Meuwly, M. Competitive reaction pathways in vibrationally induced photodissociation of H<sub>2</sub>SO<sub>4</sub>. *Phys. Chem. Chem. Phys.* **2014**, *16*, 18533–18544.
- (121) Criegee, R.; Wenner, G. Die Ozonisierung des 9, 10-Oktalins. *Justus Liebigs Ann. Chem.* **1949**, *564*, 9–15.
- (122) Alam, M. S.; Camredon, M.; Rickard, A. R.; Carr, T.; Wyche, K. P.; Hornsby, K. E.; Monks, P. S.; Bloss, W. J. Total radical yields from tropospheric ethene ozonolysis. *Phys. Chem. Chem. Phys.* **2011**, *13*, 11002–11015.
- (123) Novelli, A.; Vereecken, L.; Lelieveld, J.; Harder, H. Direct observation of OH formation from stabilised Criegee intermediates. *Phys. Chem. Chem. Phys.* **2014**, *16*, 19941–19951.
- (124) Taatjes, C. A. Criegee intermediates: What direct production and detection can teach us about reactions of carbonyl oxides. *Annu. Rev. Phys. Chem.* **2017**, *68*, 183–207.
- (125) Mauldin Iii, R.; Berndt, T.; Sipilä, M.; Paasonen, P.; Petäjä, T.; Kim, S.; Kurtén, T.;

- Stratmann, F.; Kerminen, V.-M.; Kulmala, M. A new atmospherically relevant oxidant of sulphur dioxide. *Nature* **2012**, *488*, 193–196.
- (126) Fang, Y.; Liu, F.; Barber, V. P.; Klippenstein, S. J.; McCoy, A. B.; Lester, M. I. Communication: Real time observation of unimolecular decay of Criegee intermediates to OH radical products. *J. Chem. Phys.* **2016**, *144*.
- (127) Kidwell, N. M.; Li, H.; Wang, X.; Bowman, J. M.; Lester, M. I. Unimolecular dissociation dynamics of vibrationally activated CH<sub>3</sub>CHOO Criegee intermediates to OH radical products. *Nat. Comm.* **2016**, *8*, 509–514.
- (128) Green, A. M.; Barber, V. P.; Fang, Y.; Klippenstein, S. J.; Lester, M. I. Selective deuteration illuminates the importance of tunneling in the unimolecular decay of Criegee intermediates to hydroxyl radical products. *Proc. Natl. Acad. Sci.* **2017**, *114*, 12372–12377.
- (129) Upadhyay, M.; Meuwly, M. Thermal and Vibrationally Activated Decomposition of the syn-CH<sub>3</sub>CHOO Criegee Intermediate. *ACS Earth and Space Chemistry* **2021**, in print.
- (130) Glowacki, D. R.; Orr-Ewing, A. J.; Harvey, J. N. Non-equilibrium reaction and relaxation dynamics in a strongly interacting explicit solvent: F+ CD<sub>3</sub>CN treated with a parallel multi-state EVB model. *J. Chem. Phys.* **2015**, *143*, 044120.
- (131) Dunning, G. T.; Glowacki, D.; Preston, T. J.; Greaves, S. J.; Greetham, G. M.; Clark, I. P.; Towrie, M.; Harvey, J. N.; Orr-Ewing, A. J. Vibrational relaxation and microsolvation of DF after F-atom reactions in polar solvents. *Science* **2015**, *347*, 530–533.
- (132) Åqvist, J.; Warshel, A. Simulation of enzyme reactions using valence bond force fields and other hybrid quantum/classical approaches. *Chem. Rev.* **1993**, *93*, 2523–2544.

- (133) Kamerlin, S. C.; Warshel, A. The EVB as a quantitative tool for formulating simulations and analyzing biological and chemical reactions. *Faraday Discuss.* **2010**, *145*, 71–106.
- (134) Repič, M.; Vianello, R.; Purg, M.; Duarte, F.; Bauer, P.; Kamerlin, S. C.; Mavri, J. Empirical valence bond simulations of the hydride transfer step in the monoamine oxidase B catalyzed metabolism of dopamine. *Prot. Struct. Func. Bioinf.* **2014**, *82*, 3347–3355.
- (135) Kulkarni, Y. S.; Liao, Q.; Byléhn, F.; Amyes, T. L.; Richard, J. P.; Kamerlin, S. C. Role of ligand-driven conformational changes in enzyme catalysis: modeling the reactivity of the catalytic cage of triosephosphate isomerase. *J. Am. Chem. Soc.* **2018**, *140*, 3854–3857.
- (136) Planas-Iglesias, J.; Marques, S. M.; Pinto, G. P.; Musil, M.; Stourac, J.; Damborsky, J.; Bednar, D. Computational design of enzymes for biotechnological applications. *Biotechnology Advances* **2021**, 107696.
- (137) Soloviov, M.; Meuwly, M. CO-dynamics in the active site of cytochrome c oxidase. *J. Chem. Phys.* **2014**, *140*, 04B605\_1.
- (138) Soloviov, M.; Meuwly, M. Reproducing kernel potential energy surfaces in biomolecular simulations: Nitric oxide binding to myoglobin. *J. Chem. Phys.* **2015**, *143*, 09B607\_1.
- (139) Soloviov, M.; Das, A. K.; Meuwly, M. Structural Interpretation of Metastable States in Myoglobin–NO. *Angew. Chem. Int. Ed.* **2016**, *55*, 10126–10130.
- (140) Unke, O. T.; Koner, D.; Patra, S.; Käser, S.; Meuwly, M. High-dimensional potential energy surfaces for molecular simulations: from empiricism to machine learning. *Mach. Learn. Sci. Tech.* **2020**, *1*, 013001.

- (141) Ma, A.; Dinner, A. R. Automatic method for identifying reaction coordinates in complex systems. *J. Phys. Chem. B* **2005**, *109*, 6769–6779.
- (142) Jung, H.; Covino, R.; Hummer, G. Artificial intelligence assists discovery of reaction coordinates and mechanisms from molecular dynamics simulations. *arXiv preprint arXiv:1901.04595* **2019**,
- (143) Brandt, S.; Sittel, F.; Ernst, M.; Stock, G. Machine learning of biomolecular reaction coordinates. *J. Phys. Chem. Lett.* **2018**, *9*, 2144–2150.
- (144) Chen, T.; Guestrin, C. Xgboost: A scalable tree boosting system. Proceedings of the 22nd acm sigkdd international conference on knowledge discovery and data mining. 2016; pp 785–794.
- (145) Bonk, B. M.; Weis, J. W.; Tidor, B. Machine learning identifies chemical characteristics that promote enzyme catalysis. *J. Am. Chem. Soc.* **2019**, *141*, 4108–4118.
- (146) Unke, O. T.; Brickel, S.; Meuwly, M. Sampling reactive regions in phase space by following the minimum dynamic path. *J. Chem. Phys.* **2019**, *150*, 074107.
- (147) Houston, P. L.; Nandi, A.; Bowman, J. M. A machine learning approach for prediction of rate constants. *J. Phys. Chem. Lett.* **2019**, *10*, 5250–5258.
- (148) Beck, M. H.; Jäckle, A.; Worth, G. A.; Meyer, H.-D. The multiconfiguration time-dependent Hartree (MCTDH) method: a highly efficient algorithm for propagating wavepackets. *Phys. Rep.* **2000**, *324*, 1–105.
- (149) Craig, I. R.; Manolopoulos, D. E. A refined ring polymer molecular dynamics theory of chemical reaction rates. *J. Chem. Phys.* **2005**, *123*, 034102.
- (150) Koner, D.; Unke, O. T.; Boe, K.; Bemish, R. J.; Meuwly, M. Exhaustive state-to-state cross sections for reactive molecular collisions from importance sampling simulation and a neural network representation. *J. Chem. Phys.* **2019**, *150*, 211101.

- (151) Arnold, J.; San Vicente Veliz, J. C.; Koner, D.; Singh, N.; Bemish, R. J.; Meuwly, M. Machine Learning Product State Distributions from Initial Reactant States for a Reactive Atom-Diatom Collision System. *J. Chem. Phys.* **2021**, in print.
- (152) Arnold, J.; Koner, D.; Käser, S.; Singh, N.; Bemish, R. J.; Meuwly, M. Machine Learning for Observables: Reactant to Product State Distributions for Atom–Diatom Collisions. *J. Phys. Chem. A* **2020**, *124*, 7177–7190.
- (153) Kananenka, A. A.; Yao, K.; Corcelli, S. A.; Skinner, J. Machine learning for vibrational spectroscopic maps. *J. Chem. Theor. Comp.* **2019**, *15*, 6850–6858.
- (154) Upadhyay, M.; Pezzella, M.; Meuwly, M. Genesis of Polyatomic Molecules in Dark Clouds: CO<sub>2</sub> Formation on Cold Amorphous Solid Water. *J. Phys. Chem. Lett.* **2021**, *12*, 6781–6787.
- (155) Upadhyay, M.; Meuwly, M. Energy Redistribution following CO<sub>2</sub> Formation on Cold Amorphous Solid Water. *Frontiers in Chemistry in print; arXiv:2112.00482* **2021**,
- (156) Ogryzlo, E.; Reilly, J.; Thrush, B. Vibrational excitation of CO from the reaction C+O<sub>2</sub>. *Chem. Phys. Lett.* **1973**, *23*, 37–39.
- (157) Pezzella, M.; Unke, O. T.; Meuwly, M. Molecular Oxygen Formation in Interstellar Ices Does Not Require Tunneling. *J. Phys. Chem. Lett.* **2018**, *9*, 1822–1826.
- (158) Molpeceres, G.; Zaverkin, V.; Kästner, J. Neural-network assisted study of nitrogen atom dynamics on amorphous solid water–I. adsorption and desorption. *Mon. Not. R. Astron. Soc* **2020**, *499*, 1373–1384.
- (159) Pezzella, M.; Meuwly, M. O<sub>2</sub> formation in cold environments. *Phys. Chem. Chem. Phys.* **2019**, *21*, 6247–6255.
- (160) Pezzella, M.; Koner, D.; Meuwly, M. Formation and Stabilization of Ground and

- Excited-State Singlet O<sub>2</sub> upon Recombination of <sup>3</sup>P Oxygen on Amorphous Solid Water. *J. Phys. Chem. Lett.* **2020**, *11*, 2171–2176.
- (161) Käser, S.; Boittier, E. D.; Upadhyay, M.; Meuwly, M. Transfer Learning to CCSD(T): Accurate Anharmonic Frequencies from Machine Learning Models. *J. Chem. Theor. Comp.* **2021**, *17*, 3687–3699.
- (162) Käser, S.; Meuwly, M. Transfer learned potential energy surfaces: accurate anharmonic vibrational dynamics and dissociation energies for the formic acid monomer and dimer. *Phys. Chem. Chem. Phys.* **2022**,
- (163) Zhang, L.; Wang, H.; Muniz, M. C.; Panagiotopoulos, A. Z.; Car, R.; E, W. A deep potential model with long-range electrostatic interactions. *arXiv preprint arXiv:2112.13327* **2021**,
- (164) Koner, D.; Veliz, J. C. S. V.; van der Avoird, A.; Meuwly, M. Near dissociation states for H<sub>2</sub><sup>+</sup>–He on MRCI and FCI potential energy surfaces. *Phys. Chem. Chem. Phys.* **2019**, *21*, 24976–24983.
- (165) Koner, D.; Meuwly, M. Permutationally invariant, reproducing kernel-based potential energy surfaces for polyatomic molecules: From formaldehyde to acetone. *J. Chem. Theor. Comp.* **2020**, *16*, 5474–5484.
- (166) Nandi, A.; Qu, C.; Houston, P. L.; Conte, R.; Bowman, J. M.  $\Delta$ -machine learning for potential energy surfaces: A PIP approach to bring a DFT-based PES to CCSD(T) level of theory. *J. Chem. Phys.* **2021**, *154*, 051102.
- (167) Houston, P. L.; Qu, C.; Nandi, A.; Conte, R.; Yu, Q.; Bowman, J. M. Permutationally invariant polynomial regression for energies and gradients, using reverse differentiation, achieves orders of magnitude speed-up with high precision compared to other machine learning methods. *J. Chem. Phys.* **2022**, in print.